Quantifying the dependence of drop spectrum width on cloud drop number concentration for cloud remote sensing

Matthew D. Lebsock[1], Mikael Witte[1,2]

[1]Jet Propulsion Laboratory, California Institute of Technology, Pasadena, CA, USA

5   [2]Department of Meteorology, Naval Postgraduate School, Monterey, CA, USA

Correspondence to: Matthew D. Lebsock (matthew.d.lebsock@jpl.nasa.gov)

Copyright statement. © 2023 California Institute of Technology. Government Sponsorship Acknowledged

Abstract. In-situ measurements of liquid cloud and precipitation drop size distributions from aircraft-mounted probes are used to examine the relationship of the width of drop size distributions to cloud drop number. The width of the size distribution is

10   quantified in terms of the parameter $k=(r_v/r_e)^3$, where r_v is the volume mean radius and r_e is the effective radius of the distributions. We find that on small spatial scales (~100 m), k is positively correlated with cloud drop number. This correlation is robust across a variety of campaigns using different probe technology. A new parameterization of k versus cloud drop number is developed. This new parameterization of k is used in an algorithm to derive cloud drop number in liquid phase clouds using satellite measurements of cloud optical depth and effective radius from the MODIS (Moderate Resolution

15   Imaging Spectroradiometer) sensor on Aqua. This algorithm is compared to the standard approach to derive drop number concentration that assumes a fixed value for k. The general tendency of the parameterization is to narrow the distribution of derived number concentration. The new parameterization generally increases the derived number concentration over ocean, where N is low, and decreases it over land, where N is high. Regional biases are as large as 20% with the magnitude of the bias closely tracking the regional mean number concentration. Interestingly, biases are smallest in regions of frequent

20   stratocumulus cloud cover, which are a regime of significant interest for study of the aerosol indirect effect on clouds.

1 Introduction

Satellite Visible and ShortWave InfraRed VSWIR imagers provide measurements of cloud optical depth (τ) and effective radius (r_e) using the bispectral method (Nakajima and King, 1990). There has been an abundance of literature that proposes a translation of these radiative properties to the microphysical properties, liquid water path (W) and cloud drop number (N),

25   using an adiabatic cloud model (e.g. Boers, 2006; Bennartz 2007; Grosvenor and Wood; 2014; Bennartz and Rausch, 2017). Following the adiabatic model, the number concentration can be expressed as (Grosvenor et al., 2018)

$$N = \frac{1}{2\pi k} \sqrt{\frac{5 f_{ad} c_w \tau}{Q_{ext} \rho_w r_e^5}}, \tag{1}$$

where f_{ad} is the adiabatic fraction (constrained between 0 and 1), Q_{ext} is the extinction efficiency (commonly approximated as 2 in the geometric scattering limit), c_w is the condensation rate, and ρ_w is the density of liquid water.

30   The parameter k is defined as

$$k = \left(\frac{r_v}{r_e}\right)^3,$$ (2)

where r_v is the volume mean radius and r_e is the effective radius. For a given assumption regarding the shape of the drop size distribution k can be related to various measures of the droplet spectral width. In particular, many studies evaluate the relative dispersion of the DSD defined as the standard deviation normalized by the mean radius, which can be directly related to k. For

35   realistic parameterization of the drop size distribution, k is inversely related to the relative dispersion of the DSD.

Grosvenor et al. (2018) have presented a comprehensive uncertainty analysis of N retrievals that use Equation 1. They suggest a pixel-scale uncertainty of 78%, which is dominated by uncertainty in the retrieved r_e owing to the -5/2 power to which it is raised. Note that the parameter with the second largest power in Equation 1 is k, which is raised to the -1 power. To our

40   knowledge, all published algorithms that derive N from τ and r_e have assumed a fixed value of k. The review of Grosvenor et al. (2018) propose $k = 0.8 +/- 0.1$ whereas Bennartz and Rausch (2017) suggest a 20% uncertainty in k. This intent of this paper is to revisit the uncertainty in remotely sensed N resulting from the assumption of a constant k.

The sign of the corelation between k and N is not clear in the published literature. Some analyses of probe data suggest a

45   negative correlation between k and N. For example, Martin et al., (1994) find $k = 0.67$ and $k = 0.88$ for a polluted continental cloud and clean oceanic cloud respectively. Similarly, McFarquhar and Heymfield (2001) find $k = 0.73$ and $k = 0.83$ for polluted and pristine clouds respectively. Liu and Daum (2002) show data implying a negative k-N correlation based on probe data from several field campaigns. Other analysis of probe data show a positive k-N correlation. Lu et al. (2007) show a positive k-N relationship in DSDs measured during the Marine Stratus/Stratocumulus Experiment. Brenguier et al. (2011) evaluate data

50   from five field experiments, finding no discernible k-N correlation while attributing some of the correlations reported by previous studies to instrument measurement and sampling artifacts.

Some of the disagreement in the reported k-N correlation can be explained by the spatio-temporal scale on which it is quantified. For example, Pawlowska et al. (2006) show that the relative dispersion of the DSD tends to decrease with N within

55   a given flight leg (implying a positive k-N correlation), however the sign of this relationship reverses when evaluating flight averages. Hu et al. (2021) find no correlation for inter-cloud correlation either within campaigns or across the five campaigns they analysed. However, consistent with Pawloswka et al. (2006), they find when analysing the high-resolution 1 Hz DSDs that intra-cloud relative dispersion decreases with increasing number concentration. Hu et al. (2021) further show that the variance explained in the k-N relationship exceeds 40% up to scales of 10 km and quickly decreases at scales above 30 km.

60 An analytical model based purely on the condensational growth process (Liu et al., 2006) has demonstrated that for a fixed updraft velocity an increase in CCN concentration leads to an increase in N and an increase in relative dispersion, whereas a for fixed CCN an increase in updraft velocity leads to an increase in N but a decrease in relative dispersion. The former effect is interpreted to be relevant at larger scales (inter-cloud) while the later effect is interpreted to be relevant at smaller scales (intra-cloud). Data from aircraft penetrations of non-precipitating cumulus have confirmed the positive/negative correlation of
65 updraft velocity with N/k respectively on the intra-cloud scale (Lu et al., 2012)

The above explanations do not consider the role of the collision-coalescence process. Recent observations that incorporate measurement of the radar Doppler skewness suggest that 40-50% of marine boundary layer clouds with liquid water path < 50 gm^{-2} contain drizzle drops and that drizzle is ubiquitous for thicker clouds (Zhu et al., 2022), which indicates that collision-
70 coalescence process cannot be ignored in explanations of drop size distribution broadening. A few studies have examined the effect of precipitation on the estimation of k from probe data. Wood (2000) show a reduction in k when drizzle sized drops are included in the calculation and that the ratio of the drizzle and cloud mode liquid water contents can accurately parameterize this reduction. Ackerman et al. (2000) present data from the Monterey Area Ship Track field project which demonstrate that the correlation between k and N can take either positive or negative sign. They show examples in which the sign of the
75 correlation was negative in a non-precipitating Stratocumulus with relatively large N and positive in precipitating Stratocumulus with relatively low N. Large Eddy Simulation (LES) of Stratocumulus coupled with bin microphysics shows that coalescence broadening is a key process in the development of a positive k-N correlation and that the k-N relationship is highly non-linear with the steepest slope at low values N in the presence of precipitation (Lu and Seinfeld, 2006).

80 Two points are evident in the body of literature seeking to parameterize k: (1) the spatial scale of the data is a critical determinant of the derived k-N relationship, (2) the effects of coalescence broadening have frequently been ignored. This paper specifically addresses these issues in the context of deriving N from passive VSWIR remote sensing data.

2 Data and Methods

85 ### 2.1 Probe Data

We evaluate measurements of drops size distribution from three combinations of cloud microphysical probes spanning five airborne experiments:

1. The Aerosol and Cloud Experiments in the Eastern North Atlantic (ACE-ENA) was a deployment of Atmospheric Radiation Measurement (ARM) Gulfstream-1 (G-1) between June 2017 and February 2018 around the ARM Eastern
90 North Atlantic site (Wang et al., 2022). The G-1 sampled primarily marine Stratocumulus within 50 km of the ENA site. The primary sampling strategy was an L-shaped pattern in the horizontal with the vertex at the ARM surface

site: one leg parallel to the mean PBL flow and one leg perpendicular. The vertical sampling module consisted of in-cloud level legs at cloud base, mid-cloud and cloud top followed by a sawtooth pattern between cloud top and the inversion layer above. Probe data includes the Fast Cloud Droplet Probe (FCDP) and the 2D-Stereo (2DS) Particle Imaging Probe. The FCDP measures drops of diameter 3-50 µm in bins 1.5-3 µm across (increasing with drop size). The 2DS measures drops 10<d<3000 µm in 10 μm increments. We combine the data from each probe using data from the FCDP (d < 30 µm) and 2DS (d > 30 µm).

2. The Cloud System Evolution over the Trades (CSET; Albrecht et al., 2019) sampled Stratocumulus and Cumulus clouds along Lagrangian trajectories between California and Hawaii with the National Science Foundation Gulfstream-V (G-V). The focus of the campaign was understanding the evolution of cloud, thermodynamic, and aerosol properties along the Stratocumulus to Cumulus transition. Boundary layer sampling modules were composed of a sub-cloud level leg, a cloud base level leg and a sawtooth leg between cloud top and the inversion layer above. The G-V microphysical probes include a Holographic Detector for Clouds (HOLODEC) and a 2D Cloud (2DC) probe. The HOLODEC samples drops 6<d<500 µm with bins from 4-50 µm width (increasing with drop size). The 2DC samples drops 25<d<1550 µm in 25 µm increments. We combine the data from each probe using data from the HOLODEC (d < 75 µm) and 2DC (d > 75 µm).

3. The Center for Interdisciplinary Remotely-Piloted Airborne Studies (CIRPAS) Twin Otter is frequently flown in coastal stratocumulus (Sorooshian et al. 2018). Here we examine data from two campaigns flown off the coast of Monterey, CA and one off the coast of Iquique, Chile, respectively: Marine Stratus/Stratocumulus Experiment (MASE; Lu et al. 2007); Physics Of Stratocumulus Top (POST; Witte et al. 2017); and VAMOS Ocean-Cloud-Atmosphere-Lands Study (VOCALS; Zheng et al. 2011). Level legs at cloud base, mid-cloud and cloud top were flown for MASE and VOCALS while POST primarily used sawtooth patterns from 100 m below cloud top to 100 m above. Probe data includes the Phase Doppler Interferometer (PDI) and the Cloud Imaging Probe (CIP). The PDI measures drops 2<d<100 µm in logarithmically space bins of width $d\log_{10}d=0.0156$. The CIP is essentially identical to the 2DC probe used in CSET and samples drops 25<d<1550 µm in 25 µm increments. We combine the data from each probe using data from the PDI (d<75 µm) and CIP (d>75 µm).

Figure 1 shows an example of a merged DSD from each of the three probe combinations.
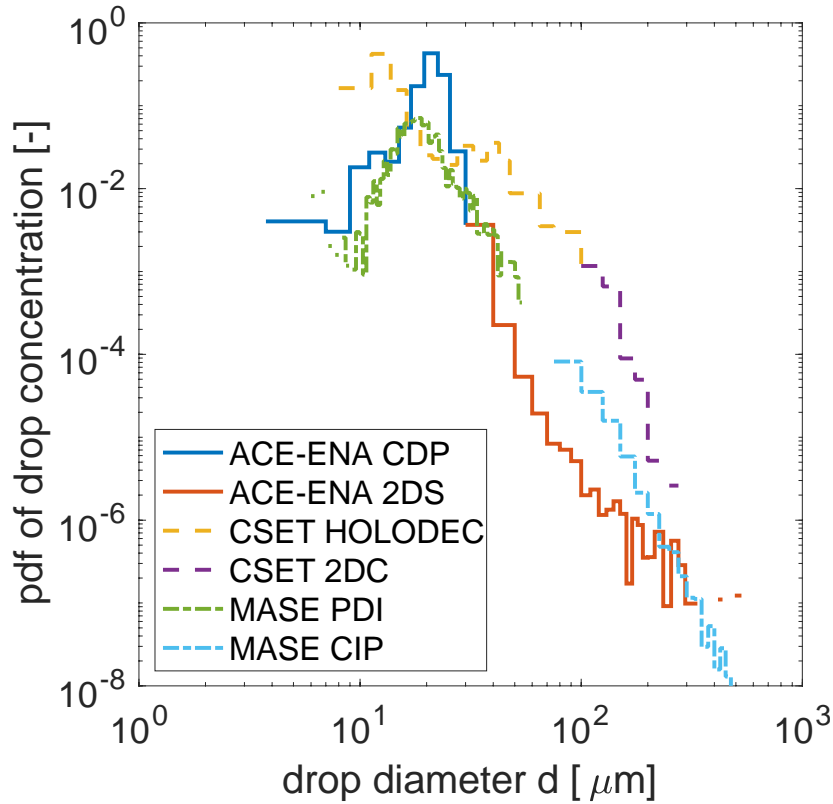
120 **Figure 1: An example of merged drop size distributions from each campaign.**

For each 1 Hz DSD, several microphysical quantities are calculated. The number concentration is calculated as

$$N = \sum_{r_{min}}^{r_{max}} n(r)\Delta r. \tag{3}$$

Liquid water content is calculated as

125 $$l = \frac{4}{3}\rho_l \pi \sum_{r_{min}}^{r_{max}} n(r)r^3\Delta r. \tag{4}$$

The volume mean radius is calculated as

$$r_v = \left(\frac{3l}{4\pi\rho_l N}\right)^{1/3}. \tag{5}$$

The effective radius is defined as

$$r_e = \frac{\sum_{r_{min}}^{r_{max}} N(r)r^3\Delta r}{\sum_{r_{min}}^{r_{max}} N(r)r^2\Delta r}. \tag{6}$$

130 Each quantity is calculated three times for the cloud mode, precipitation mode, and total DSD. A threshold radius of 27.5 μm is used to separate the cloud and precipitation modes. The parameter k is further derived from the calculated r_v and r_e. In doing so a decision must be made as to whether to include precipitation sized drops in the calculation. In principle, VSWIR imagers see the radiative effects of the entire drop size distribution. However, the SWIR bands from which the measurement of r_e are

derived are heavily weighted towards cloud top (Platnick, 2000). Gravitational settling effectively removes most large drops from the cloud top, therefore here we make the assumption that only the cloud-mode drops ($r < 27.5\ \mu$m) contribute to the radiatively effective k.

We perform filtering of the data to ensure robust sampling of the cloud mode DSD. We require $l_c > 0.01$ gm^{-3}, $N_c > 0.1$ cm^{-3}, and at least three of the cloud mode bins have non-zero counts. We further perform additional filtering of the data to ensure that we are sampling cloudy liquid-phase volumes as opposed to sub-cloud drizzle or ice cloud. Specifically, we require relative humidity $> 98\%$, temperature > 273.15 K, and aircraft altitude > 700 m. After filtering there are 157,117 DSDs including 13,205 from CSET, 90,172 DSDs ACE-ENA, and 53,740 from the PDI dataset. Of these 31% have precipitation water content greater than 0.01 gm^{-3}.

2.2 Satellite Data

This study uses the collection 6 MODIS cloud products from Aqua subset to a 15 pixel (± 5 km) swath centered on the CloudSat ground track called MAC06S0 (Savtchenko et al. 2008). These files contain the same data fields as their parent product, MYD06 (Platnick et al. 2017). Data from 2007-2016 are used. Equation 1 is used to derive the cloud drop number concentration using the effective radius derived from the MODIS band 20, 3.7 μm channel. Only single layer liquid phase clouds are considered. Cloud phase is determined from the MODIS cloud phase optical properties flag. The parameter f_{ad} is set to 0.66 following Grosvenor et al., 2018 and the condensation rate is expressed as,

$$c_w = \rho_{air} \frac{c_p}{L_v} (\Gamma_d - \Gamma_m) \tag{7}$$

where ρ_{air} is the density of air, c_p is the specific heat of dry air at constant pressure, L_v is the latent heat of vaporization, Γ_d is the dry adiabatic lapse rate, and Γ_m is the moist adiabatic lapse rate. Calculation of c_w requires an estimate of cloud base temperature, which we take as the temperature at the Lifting Condensation Level (LCL) estimated from weather analysis fields from the ECMWF-aux (Partain and Cronk, 2017) pressure and temperature fields, which is a weather analysis interpolated in space and time to the CloudSat data. The details of this calculation are provided in Appendix A. Two representations of k are used; we compare a fixed value of $k = 0.8$ with a parameterization of k based on N derived from probe data in Section 3.1.

3 Results

3.1 Drop Size Distribution Properties

We begin by showing the distributions of microphysical variables for the three datasets in Figure 2. The range of cloud drop number spans 0-500 cm^{-3}. The PDI dataset is weighted towards higher N while the FCDP and especially the HOLODEC datasets are weighted towards the lowest N. These differences are a consequence of the geographic regimes sampled by the

165 different campaigns: the CIRPAS Twin Otter is constrained to fly near the coast and the associated natural and anthropogenic aerosol sources, while much of the boundary layer sampling in CSET took place over extremely clean remote oceanic regions. The corresponding effective radii distributions range between roughly $5 - 25$ μm. Cloud liquid water content distributions are similar across the datasets, with a broad range of values from the artificial cut off at 0.01 gm^{-3} to greater than 1 gm^{-3}. The distributions of k show that the PDI have the largest k followed by the FCDP and then the HOLODEC. The mean value of k is

170 0.8, which is consistent with the recommended value of Grosvenor et al., 2018, however there is a large spread and the distributions are negatively skewed with values below 0.6 not uncommon.
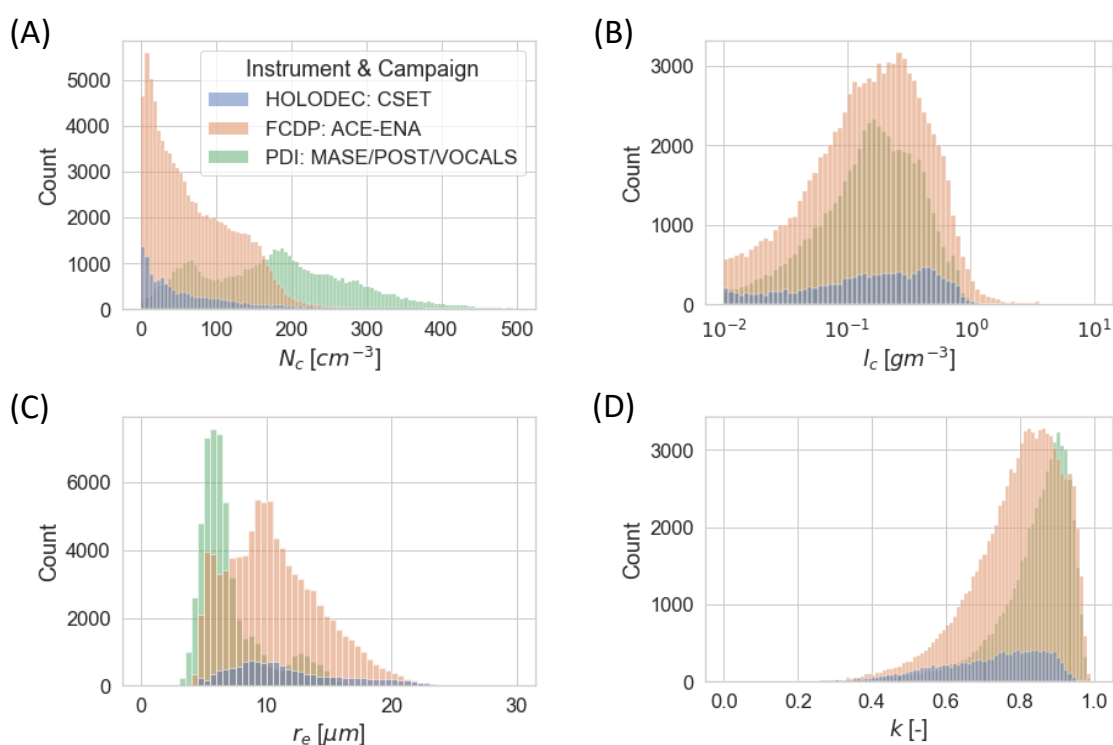
Figure 2: Distribution of cloud drop number (A), cloud liquid water content (B), effective radius (C), and *k* (D) for the three datasets.

175

We now turn to the relationship between N and k. Figure 3 shows the mean DSDs for each dataset sorted by the cloud drop number concentration. Here we include two filters applied to the data; The first includes all DSDs (Panels A-C), while the second includes only DSD's that have no water in the precipitation mode (Panels D-F). Note that the calculation of k is only based on the cloud mode drops ($r < 27.5$ μm) even for the DSDs that do have precipitation sized drops. Including precipitation

180 sized drops in the calculation (not shown) results in significantly smaller values of k consistent with Wood (2000), however as discussed in Section 2.1 we believe that including precipitation sized drops is not appropriate in the context of the remote

sensing application. There are some clear biases in the data. First, the FCDP data from ACE-ENA show consistently low counts in several bins around 6 μm radius. This minimum is not observed in the DSD's from the other datasets nor is there any microphysical reason to expect this feature. Second, the CSET DSD's are limited by an inability to sample the smallest drops. Third, the PDI data shows noisiness in the smallest bins. Despite these artifacts, there is a clear broadening signature as N decreases in all of the DSDs, which use completely different probes and sample different cloud regimes. The broadening is most obvious in the drizzle sized drops but is also clearly present in the cloud-size drops (Panels A-C). It is also apparent in the DSD's that have no precipitation water (Panels D-F). Furthermore, these results are robust when controlling for variation in the cloud liquid water content (Figure S1).
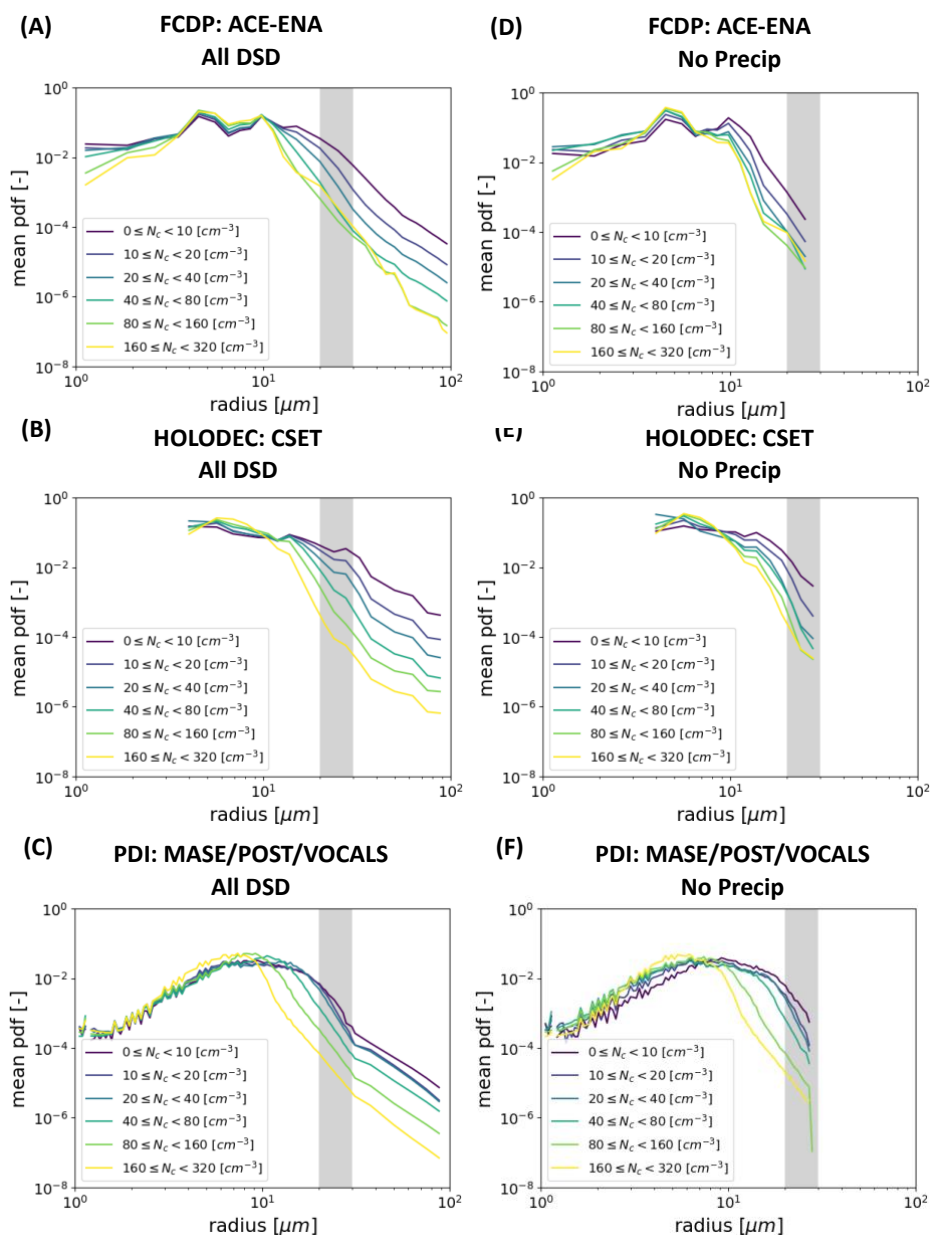
Figure 3: The mean probability density function (pdf) of the drop concentration sorted by the cloud mode drop number concentration for the three datasets. Panels A-C show results for all DSDs and panels D-F shows results filtered for DSDs with no precipitation water. The parameter k is calculated using only the cloud-sized drops even when precipitation is present in the DSD. The grey bar shows a notional range of radius 20-30 μm separating cloud from precipitation sized drops.

Figure 4 shows the dependence of k on N for each of the three datasets. Panel A shows the results for non-precipitating DSDs, while panel B is filtered for only precipitating DSDs. The increase of k with N is clear across all three datasets. The median values increase from around 0.6 to 0.9 across the range of N from $0 – 500$ cm^{-3}. The variability around this mean value is large for small N but decreases consistently as N increases. The general relationship is consistent across all three datasets however there are some quantitative differences especially for the lowest N where the HOLODEC data have smaller k values than either the FCDP or the PDI data. It is possible that this low bias in HOLODEC results from the inability to sample the smallest drops, however this is not guaranteed. For example, revisiting Figure 3, it is clear that the smallest drops increase the DSD width for the FCDP data but decrease it for the PDI data. More work is warranted to resolve the differences between the probes with regards to the N-dependence of the sampling of smallest drops. Returning to Figure 4, the dependence of k on N appears regardless of the presence of precipitation in the DSDs, however, there is a tendency for k to be larger (narrower DSD) when the precipitating DSDs are removed, which is particularly evident at low values of N. This effect is especially evident in the CSET HOLODEC data which happens to be the dataset with the lowest number concentration. This suggests, that although collision-coalescence is not necessary to explain the observed k-N correlation it likely plays a role in strengthening that correlation.
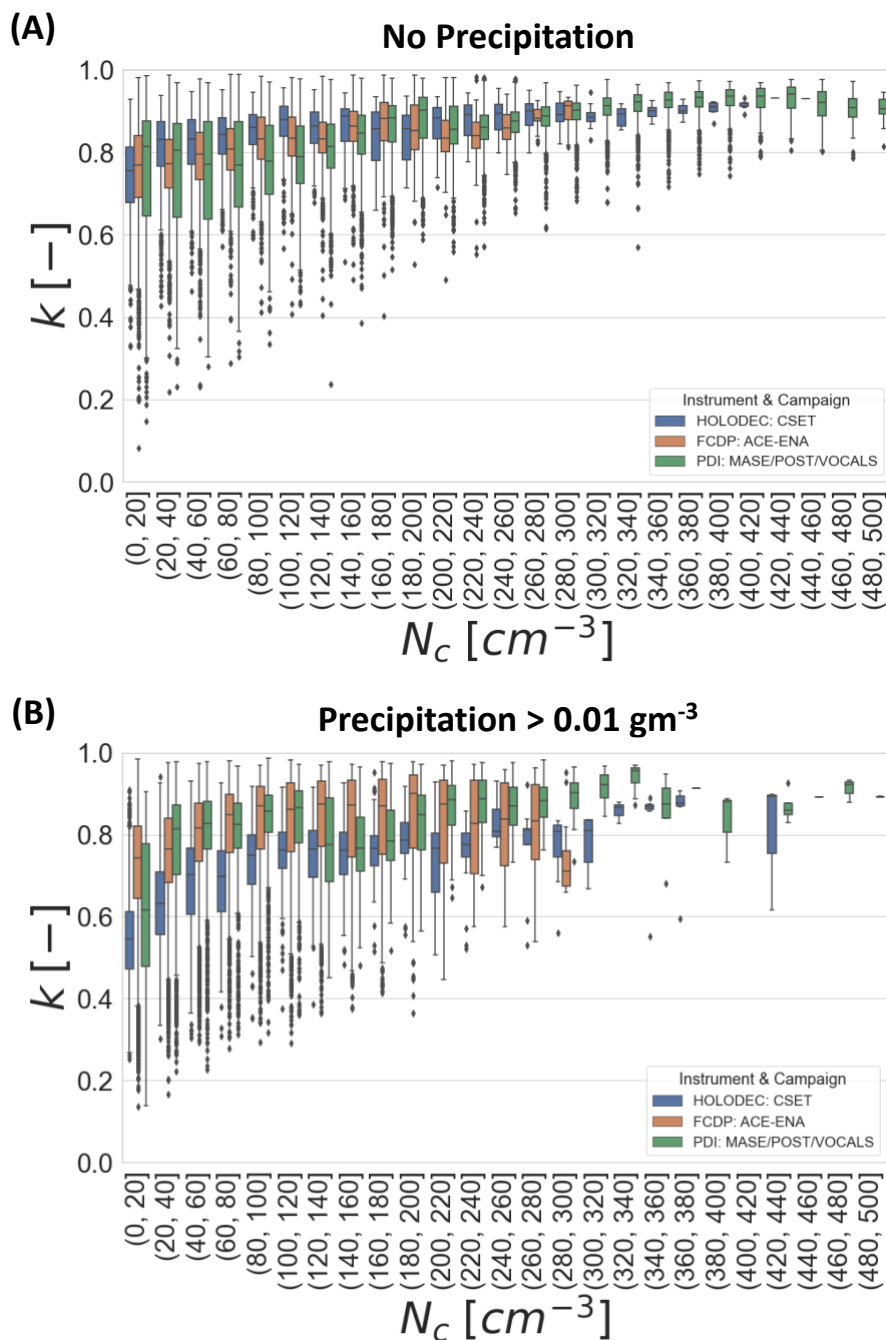
Figure 4: Box and whisker plot shows the distribution quartiles and outliers of *k* as a function of *N* for the three different instruments.
215 **Panel A shows results for non-precipitating DSDs and panel B shows results filtered for DSDs with precipitation water. The parameter *k* is calculated using only the cloud-sized drops even when precipitation is present in the DSD.**

Given these results, we propose the following parameterization for the N-dependence of k for clouds

$$k(N) = k_B + (k_T - k_B)\left(\frac{N}{N+N^*}\right),\tag{8}$$

with $0 \le k_B < k_T \le 1$, $N^* > 0$. This functional form is bounded between k_B and k_T and increases monotonically but fastest at low N, as we observe in the data. We use the python curvefit package to implement the Levenberg-Marquardt method to perform a non-linear least-squares regression to fit the parameters of Equation 8 for each dataset individually, and for a weighted-combined dataset. Fitting parameters are shown in Table 1. The weighting in the combined data is given by $1/\sqrt{M}$ where M is the sample count for each dataset. In the absence of this weighting the combined fit is nearly identical to the ACE-ENA fit, which has the largest sample size. The raw data and the curve fits are shown in Figure 5. All of the fits show a clear positive correlation between N and k, however the PDI and FCDP k values are larger than the CSET values, particularly for the smallest N. In contrast the PDI data and the ACE-ENA have larger values of k at large N. By design, the combined fit falls in the middle of the distributions. Given the limitations of each of the probe datasets (e.g. Figure 3) and the limited sampling of the datasets used here, we take this combined fit as our best-estimate parameterization of $k(N)$.
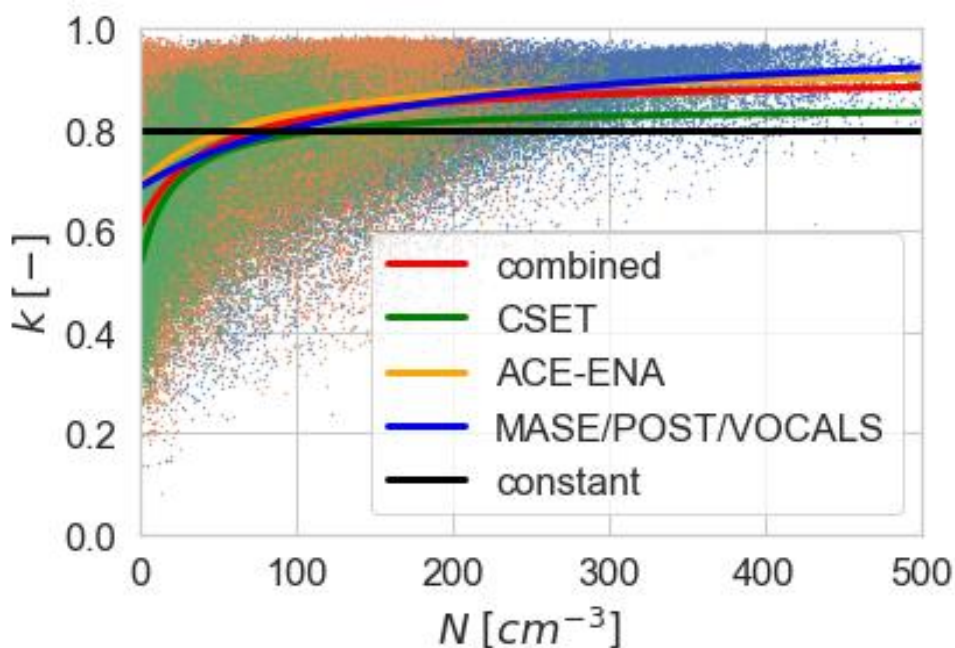
Figure 5: Curve fits for Equation 7 to the data from each of the three data sets as well as a weighted combined dataset. The weighting normalizes the influence of each of the three datasets due to the dramatically different number of data points in each dataset.

Table 1: Fitting parameters for Equation 7.

	k_B	k_T	N^*
Combined	0.61	0.90	43
HOLODEC: CSET	0.53	0.85	22
FCDP: ACE-ENA	0.69	0.94	73
PDI: MASE/POST/VOCALS	0.68	1.0	163

3.2 Satellite Retrievals

240

Here we incorporate the new parameterization of k into retrievals of N. To begin, we write Equation 1 as

$$N = \frac{\phi(\tau, r_e)}{k(N)}. \tag{9}$$

Plugging in Equation 8 for $k(N)$ and rearranging terms results in the quadratic equation

$$k_T N^2 + (k_B N^* - \phi)N - \phi N^* = 0. \tag{10}$$

245   Employing the quadratic formula and taking the positive root, gives the following solution for N,

$$N = \frac{\phi - k_B N^* + \sqrt{(k_B N^* - \phi)^2 + 4 k_T \phi N^*}}{2 k_T}. \tag{11}$$

Equation 11 is specific to the parametric form of $k(N)$ provided in Equation 8, however we note that if k is an arbitrary monotonic function of N, an iterative solution can also be employed to solve for N. In the results that follow we use the parameters for the combined fit for $k(N)$ given in Table 1.

250

Figure 6 shows N as a function of τ and r_e derived from Equation 11, along with the bias in the derived N caused by ignoring the parameterized k-N correlation. The parameterization decreases N for the largest values and increases it for the smallest values. Over the range of τ and r_e shown the bias varies between roughly -10 % and 30 %. The sign of the bias switches near the value of 81.7 cm⁻³. The co-distributions of the observed MODIS r_e and τ that are used in this study are also overlaid on

255   these plots. Note in Figure 6B that these observed distributions span the range of positive and negative bias, with a tendency to lie near the zero-bias ridge. A result is that the mean bias in derived N caused by ignoring k-N correlation will be small even if it can be significant in the case of the extreme values.
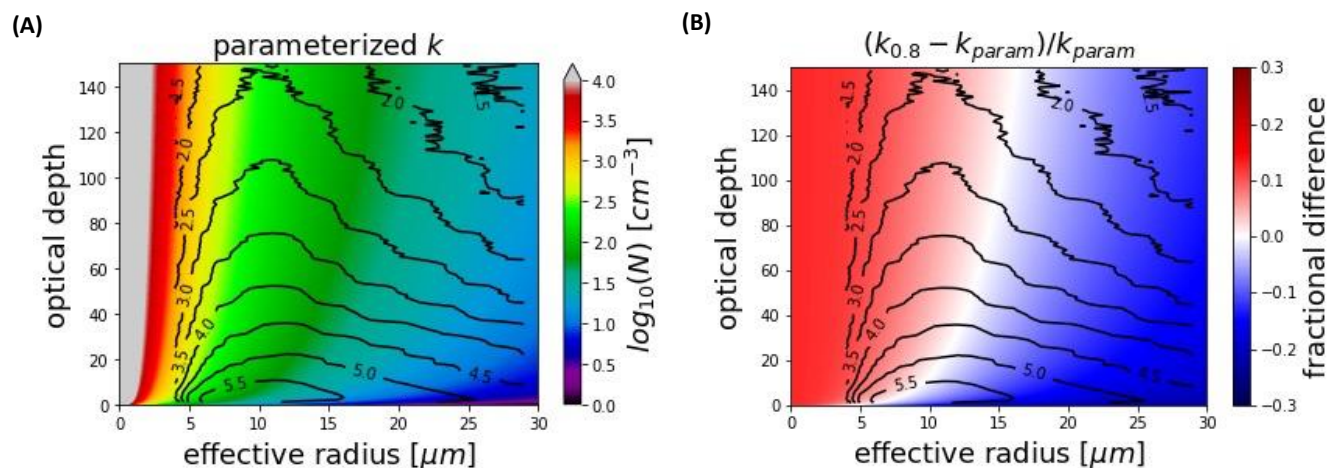
260

Figure 6: Derived N using the parameterized k and $c_w = 0.004$ gm^{-4} (A) and bias between the parameterized k and constant k retrievals (B). The black contours show the base 10 logarithm of the counts of the observed MODIS effective radius and optical depth used in the study.

265 Figure 7 shows the regional pattern of N derived using the k-N parameterization in panel A. Implementing the parameterization makes essentially no difference in the qualitative understanding of the distribution of N globally. The mean N tends to be lowest over remote ocean areas, increasing in regions of low altitude stratocumulus over ocean, and highest over populated regions over land. Nevertheless, there are subtle quantitative difference in the retrieved N when using the parameterized k. The Root-Mean-Square-Deviation can be as large as 20% in regions of low mean N. Importantly, the RMSD is smallest in the

270 regions of stratocumulus off the west coasts of the continents and in the mid-latitude storm tracks. This results from the fact that the k-N parameterization is near $k = 0.8$ given the mean N in these cloud regimes. This result explains why assuming a constant $k = 0.8$ tends to work reasonably well, since these are the regimes that contribute the bulk of the observed low cloud retrievals by the VSWIR sensors. Finally, the regional distribution of uncertainties are reflected in a bias in the mean which approaches -20% in remote ocean areas and is smaller than about 5% in polluted areas over land.
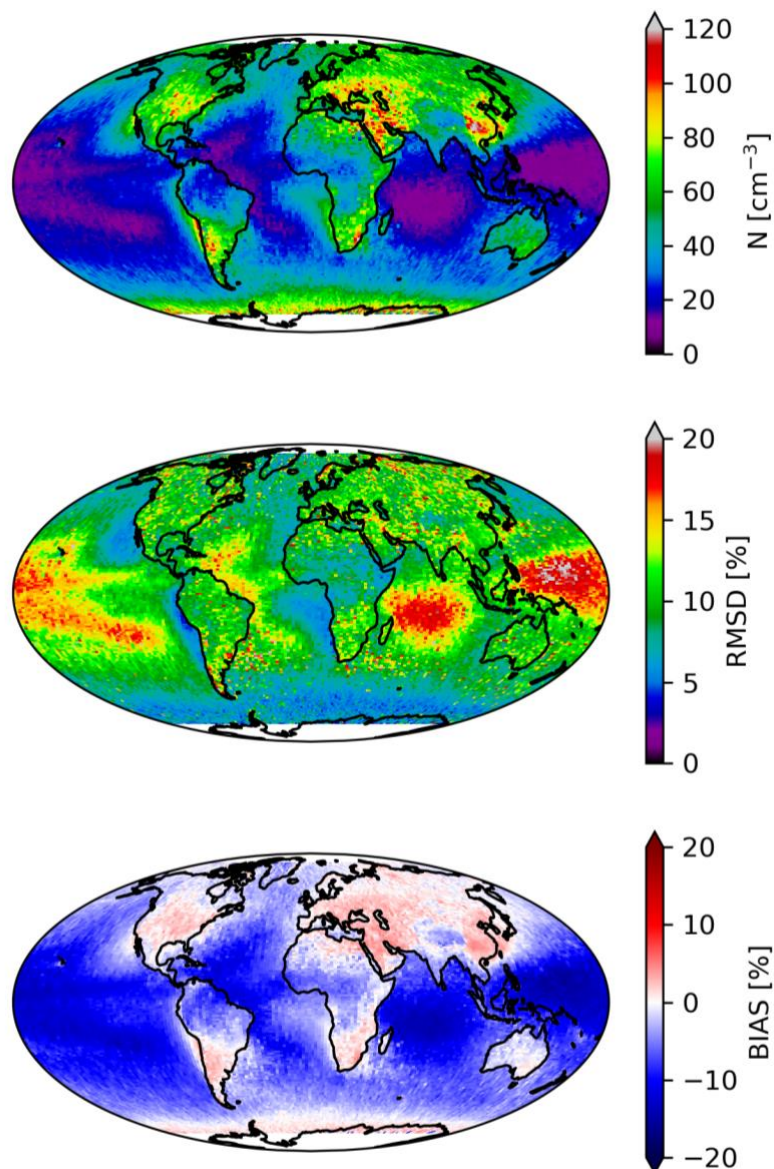
Figure 7: Derived *N* using the parameterized *k* (A), Root-Mean-Square-Deviation (RMSD) between parameterized and constant k retrievals (B), and mean bias between the parameterized *k* and constant *k* retrievals (C). Here Bias is defined as a bias of the constant k retrieval relative to a variable k retrieval.

4 Summary and Discussion

We have quantified the dependence of a parameter describing the droplet spectrum width (*k*) on the cloud droplet number concentration (*N*). We specifically address this dependence at the small spatial scales relevant to cloud remote sensing by using

1 hZ data that corresponds to approximately a 100 m spatial scale. We find that, using the high-frequency data, k and N are positively correlated, which is in agreement with a number of recent studies. This finding is robust across 5 different campaigns employing three different drop measurement technologies. The sign of this correlation is consistent with theoretical

285 expectations that at small scales, variation in vertical velocity within a cloud, affect the supersaturation in a manner that induce a positive k-N correlation (Liu et al., 2006). We have further shown here that when the drop size distributions are sorted by the presence of precipitation, the distribution of k broadens, and the slope of the k-N correlation increases. This finding points to the added importance of the collision-coalescence process in droplet spectrum broadening, which is consistent with large eddy simulations coupled to bin microphysics (Lu and Seinfeld, 2006).

290

Based on these findings, a parameterization of k given N is presented for use in satellite remote sensing of the droplet number concentration. This parameterization can easily be incorporated into the existing techniques to derive N from VSWIR imagery. We show that imposing the positive k-N correlation tends to narrow the distribution of retrieved N by increasing the smallest values and decreasing the largest values. The parameterization is applied to retrievals of N using data from Aqua-MODIS. The

295 fractional bias in the remotely sensed number concentration approaches -20% in areas of the remote ocean where number concentrations are low. A smaller positive bias is found over polluted land regions. We do emphasize that the absolute magnitude of the bias in N tends to be relatively small, on the order of 1-2 cm^{-3}. Nevertheless, the data are robust in showing that there is a positive k-N correlation and employing this dependence in retrievals is relatively straightforward. Therefore, we argue that these findings inform the implementation of future retrievals of drop number concentration from satellite remote

300 sensing.

Appendix A

Calculation of the moist adiabatic condensation rate requires an estimate of the difference between the dry and moist adiabatic lapse rates and the density of air. The dry adiabatic lapse rate is,

$$\Gamma_d = \frac{g}{c_p} \tag{A1}$$

305 where g is the gravitational acceleration and c_p is the specific heat at constant pressure of dry air. The moist adiabatic lapse rate is given by,

$$\Gamma_m = g\frac{1+\frac{L_v r_v}{R_d T}}{c_p+\frac{L_v^2 r_v \epsilon}{R_d T^2}} \tag{A2}$$

where L_v is the latent heat of vaporization, r_v is the mixing ratio of water vapor, T is the temperature, and R_d is the gas constant for dry air. To include the temperature dependence in gamma we estimate cloud-base temperature as the temperature at the

310 LCL. We calculate the LCL height (Z_{LCL}) following Bolton (1980) from the surface relative humidity (RH)

$$Z_{LCL} = \frac{1}{\Gamma_d}\left(T - 55 - \left(\frac{1}{T-55} - \frac{\ln(RH)}{2840}\right)^{-1}\right) \tag{A3}$$

where the *RH* varies between 0 and 1 and the *T* is in K. The surface *RH* is calculated from the ECMWF specific humidity (q)

$$RH = \frac{q}{q_{sat}} \tag{A4}$$

and the saturation specific humidity (q_{sat}) is calculated from the saturation water vapor mixing ratio (r_{sat})

315
$$q_{sat} = \frac{r_{sat}}{1+r_{sat}} \tag{A5}$$

which in turn is calculated from the saturation vapor pressure (e_{sat}) and the surface Pressure (P)

$$r_{sat} = \epsilon \frac{e_{sat}}{P-e_{sat}} \tag{A6}$$

where $\epsilon = 0.622$. The saturation vapor pressure is calculated following the Tetens formula

$$e_{sat} = 6.1078 e^{\frac{17.269388T}{T+237.3}} \tag{A7}$$

320 Where T is degrees Celsius and e_{sat} in mb. The temperature at the LCL is calculated assuming a dry adiabatic lapse rate using the ECMWF 2-meter temperature

$$T_{LCL} = T_{2m} - \Gamma_d Z_{LCL} \tag{A8}$$

The pressure at the LCL is calculated using the surface pressure and a scale height ($Z^* = 8\ km$)

$$P_{LCL} = P_0 e^{-Z_{LCL}/Z^*} \tag{A9}$$

325 The air density at the LCL is calculated

$$\rho_{air,LCL} = \frac{P_{LCL}}{R_d T_{LCL}} \tag{A10}$$

Finally, the water vapor mixing ratio at the LCL, needed in A2, is assumed to be the saturated mixing ratio and is calculated A6 and A7 using the T_{LCL} and P_{LCL}.

Data Availability

330 *CloudSat* and MODIS data used in this study were downloaded from the CloudSat Data Processing Center (http://www.cloudsat.cira.colostate.edu/). Drop size distribution data will be made available on JPL's open repository.

Author Contribution

M.W. compiled the drop size distribution data and merged the cloud and precipitation distributions. M.L. evaluated the drop size distributions, implemented the retrieval, and prepared the manuscript.

335 **Competing Interests**

The authors have the following competing interests: At least one of the (co-)authors is a member of the editorial board of Atmospheric Chemistry and Physics.

Acknowledgments

This work was performed at the Jet Propulsion Laboratory, California Institute of Technology, under a contract with the
340   National Aeronautics and Space Administration and was funded by the *CloudSat* mission.

References

Ackerman, A. S., Toon, O. B., Taylor, J. P., Johnson, D. W., Hobbs, P. V., & Ferek, R. J.: Effects of Aerosols on Cloud
Albedo: Evaluation of Twomey's Parameterization of Cloud Susceptibility Using Measurements of Ship Tracks, Journal of
the Atmospheric Sciences, 57(16), 2684-2695, 2000.

345

Albrecht, B. A., et al.: Cloud System Evolution in the Trades (CSET): Following the evolution of boundary layer cloud systems
with the NSF–NCAR GV, Bull. Amer. Meteor. Soc., 100, 93–121, https://doi.org/10.1175/BAMS-D-17-0180.1, 2019.

Bennartz, R: Global assessment of marine boundary layer cloud droplet number concentration from satellite, Journal of
350   Geophysical Research, **112**, D02201. https://doi.org/10.1029/2006JD007547, 2007.

Bennartz, R., & Rausch, J: Global and regional estimates of warm cloud droplet number concentration based on 13 years of
AQUA-MODIS observations, Atmos. Chem. Phys., 17(16), 9815– 9836. https://doi.org/10.5194/acp-17-9815-2017, 2017.

355   Boers, R., Acarreta, J. R., & Gras, J. L.: Satellite monitoring of the first indirect aerosol effect: Retrieval of the droplet
concentration of water clouds, Journal of Geophysical Research, 111, D22208. https://doi.org/10.1029/2005JD006838, 2006.

Bolton, D.: The computation of equivalent potential temperature, *Mon. Wea. Rev.*, **108**, 1046–1053, doi:10.1175/1520-
0493(1980)108<1046:TCOEPT>2.0.CO;2, 1980.
360

Brenguier, J.-L., Burnet, F., and Geoffroy, O.: Cloud optical thickness and liquid water path – does the *k* coefficient vary with
droplet concentration?, Atmos. Chem. Phys., 11, 9771–9786, https://doi.org/10.5194/acp-11-9771-2011, 2011.

Grosvenor, D. P. and Wood, R.: The effect of solar zenith angle on MODIS cloud optical and microphysical retrievals within
365   marine liquid water clouds, Atmos. Chem. Phys., 14, 7291–7321, https://doi.org/10.5194/acp-14-7291-2014, 2014.

Grosvenor et al.: Remote sensing of droplet number concentration in warm clouds: A review of the current state of knowledge
and perspectives, Reviews of Geophysics, 56, 409– 453. https://doi.org/10.1029/2017RG000593, 2018.

370 Hu, A. Z., Igel, A. L., Chuang, P. Y., & Witte, M. K.: Recognition of inter-cloud versus intra-cloud controls on droplet dispersion with applications to microphysics parameterization, Journal of Geophysical Research: Atmospheres, 126, e2021JD035180. https://doi.org/10.1029/2021JD035180, 2021.

Liu, Y., Daum, P.: Indirect warming effect from dispersion forcing, Nature, 419, 580–581. https://doi.org/10.1038/419580a,
375 2002.

Liu, Y.,, Daum, P. and Yum S.: Analytical expression for the relative dispersion of the cloud droplet size distribution, Geophys. Res. Lett., 33, L02810, doi:10.1029/2005GL024052, 2006.

380 Lu, M.-L., and Seinfeld, J. H.: Effect of aerosol number concentration on cloud droplet dispersion: A large-eddy simulation study and implications for aerosol indirect forcing, J. Geophys. Res., 111, D02207, doi:10.1029/2005JD006419, 2006.

Lu, M.-L., Conant, W. C., Jonsson, H. H., Varutbangkul, V., Flagan, R. C., and Seinfeld, J. H.: The Marine Stratus/Stratocumulus Experiment (MASE): Aerosol-cloud relationships in marine stratocumulus, J. Geophys. Res., 112,
385 D10209, doi:10.1029/2006JD007985, 2007.

Lu, C., Liu, Y., Niu, S., and Vogelmann, A. M.: Observed impacts of vertical velocity on cloud microphysics and implications for aerosol indirect effects, Geophys. Res. Lett., 39, L21808, doi:10.1029/2012GL053599, 2012.

390 Martin, G. M., Johnson, D. W., and Spice, A: The Measurement and Parameterization of Effective Radius of Droplets in Warm Stratocumulus Clouds, J. of Atmos. Sci., 51(13), 1823-1842. https://journals.ametsoc.org/view/journals/atsc/51/13/1520-0469_1994_051_1823_tmapoe_2_0_co_2.xml, 1994.

McFarquhar, G. M., and Heymsfield, A. J.: Parameterizations of INDOEX microphysical measurements and calculations of
395 cloud susceptibility: Applications for climate studies, J. Geophys. Res., 106(D22), 28675– 28698, doi:10.1029/2000JD900777, 2001.

Morrison, H. and Grabowski, W. W.: Comparison of bulk and bin warm-rain microphysics models using a kinematic framework, J. Atmos. Sci., 64, 2839–2861, 2007.
400

Nakajima, T., & King, M.: Determination of the optical thickness and effective particle radius of clouds from reflected solar radiation measurements. Part I: Theory, J. of Atmos. Sci., 47, 1878– 1893. https://doi.org/10.1175/1520-0469(1990)047<1878:DOTOTA>2.0.CO;2, 1990.

405 Partain P., and H. Cronk: CloudSat ECMWF-AUX Auxillary Data Product Process Description and Interface Control Document, California Institute of Techology Jet Propulsion Laboratory CloudSat Project Document. https://www.cloudsat.cira.colostate.edu/cloudsat-static/info/dl/ecmwf-aux/ECMWF-AUX_PDICD.P_R05.rev0_.pdf, 2017.

Pawlowska, H., Grabowski, W. W., and Brenguier, J.-L.: Observations of the width of cloud droplet spectra in
410 stratocumulus, Geophys. Res. Lett., 33, L19810, doi:10.1029/2006GL026841, 2006.

Platnick, S.: Vertical photon transport in cloud remote sensing problems, J. Geophys. Res., 105(D18), 22919– 22935, doi:10.1029/2000JD900333, 2000.

415 Platnick, S. et al.: The MODIS Cloud Optical and Microphysical Products: Collection 6 Updates and Examples From Terra and Aqua, IEEE Trans. Geosci. Remote Sens., **55**, 502–525, https://doi.org/10.1109/TGRS.2016.2610522, 2017.

Rotstayn, L. D., & Liu, Y.: Sensitivity of the first indirect aerosol effect to an increase of cloud droplet spectral dispersion with droplet number concentration, J. Clim., 16(21), 3476– 3481. https://doi.org/10.1175/1520-
420 0442(2003)016<3476:SOTFIA>2.0.CO;2, 2003.

Rotstayn, L. D., and Liu, Y.: Cloud droplet spectral dispersion and the indirect aerosol effect: Comparison of two treatments in a GCM, Geophys. Res. Lett., 36, L10801, doi:10.1029/2009GL038216, 2009.

425 Savtchenko, A., R. Kummerer, P. Smith, A. Gopalan, S. Kempler, and G. Leptoukh: A-Train Data Depot: Bringing Atmospheric Measurements Together, IEEE Trans. Geosci. Remote Sens., 46, 2788–2795, https://doi.org/10.1109/TGRS.2008.917600, 2008.

Sorooshian, A. et al.: A multi-year data set on aerosol-cloud-precipitation-meteorology interactions for marine stratocumulus
430 clouds, Sci. Data 5, 180026. https://doi.org/10.1038/sdata.2018.26, 2018.

Wang J., R. Wood, M. Jensen, J. Chiu, Y. Liu, K. Lamer, N. Desai, S. Giangrande, D. Knopf, P. Kollias, A. Laskin, X. Liu, C. Lu, D. Mechem, F. Mei, M. Starzec, J. Tomlinson, Y. Wang, S. Yum, G. Zheng, A. Aiken, E. Azevedo, Y. Blanchard, S. China, X. Dong, F. Gallo, S. Gao, V. Ghate, S. Glienke, L. Goldberger, J. Hardin, C. Kuang, E. Luke, A. Matthews, M. Miller,
435 R. Moffet, M. Pekour, B. Schmid, A. Sedlacek, R. Shaw, J. Shilling, A. Sullivan, K. Suski, D. Veghte, R. Weber, M. Wyant, J. Yeom, M. Zawadowicz, and Z. Zhang: Aerosol and Cloud Experiments in the Eastern North Atlantic (ACE-ENA). Bull. Amer. Meteor. Soc., 103(2), 10.1175/BAMS-D-19-0220.1, 2022.

Witte, M.K., Ayala, O., Wang, L.-P., Bott, A. and Chuang, P.Y.: Estimating collision–coalescence rates from *in situ* observations of marine stratocumulus. Q.J.R. Meteorol. Soc, 143: 2755-2763. https://doi.org/10.1002/qj.3124, 2017.

Wood, R.: Parametrization of the effect of drizzle upon the droplet effective radius in stratocumulus clouds. Q.J.R. Meteorol. Soc., 126: 3309-3324. https://doi.org/10.1002/qj.49712657015, 2000.

Xie, X., Zhang, H., Liu, X., Peng, Y., & Liu, Y.: Sensitivity study of cloud parameterizations with relative dispersion in CAM5.1: Impacts on aerosol indirect effects. *Atmospheric Chemistry and Physics*, **17**(9), 5877– 5892. https://doi.org/10.5194/acp-17-5877-2017, 2017.

Zheng, X., Albrecht, B., Jonsson, H. H., Khelif, D., Feingold, G., Minnis, P., Ayers, K., Chuang, P., Donaher, S., Rossiter, D., Ghate, V., Ruiz-Plancarte, J., and Sun-Mack, S.: Observations of the boundary layer, cloud, and aerosol variability in the southeast Pacific near-coastal marine stratocumulus during VOCALS-REx, Atmos. Chem. Phys., 11, 9943–9959, https://doi.org/10.5194/acp-11-9943-2011, 2011.

Zhu, Z., Kollias, P., Luke, E., and Yang, F.: New insights on the prevalence of drizzle in marine stratocumulus clouds based on a machine learning algorithm applied to radar Doppler spectra, Atmos. Chem. Phys., 22, 7405–7416, https://doi.org/10.5194/acp-22-7405-2022, 2022.